JOURNAL OF PROPULSION AND POWER
Vol. 11, No. 6, November–December 1995

Measurements of OH and H_2O for Reacting Flow in a Supersonic Combusting Ramjet Combustor

Terence E. Parker,* Mark G. Allen,† Richard R. Foutter,‡ David M. Sonnenfroh,§ and W. Terry Rawlins¶
Physical Sciences, Inc., Andover, Massachusetts 01810

Mixing and combusting high-enthalpy flows, similar to those encountered in supersonic combusting ramjet engines, were investigated using a shock tunnel to produce the flow in conjunction with nonintrusive optical diagnostics that monitored the performance of two injector configurations. The shock tunnel was configured to produce Mach 3 flow and stagnation enthalpies corresponding to flight equivalent Mach numbers between 7–11. A pulsed hydrogen injection capability and interchangeable injector blocks provided a means of examining high-speed, high-enthalpy reacting flows. Planar laser induced fluorescence of OH radicals in the near-injector region produced images that show the combusting and mixing zones for the reacting flow. Line-of-sight exit plane measurements of water concentration and temperature were used to provide a unique method of monitoring exit plane products. Near-injector mixing dynamics and exit plane compositions were compared for wall jet and axial injection systems. In addition, exit plane measurements indicated that a quasi-steady-state condition was achieved during the 1- to 2-ms test times.

Introduction

THE development of supersonic combusting ramjet (SCRAMJET) engines requires testing using new, nonintrusive methods in high-speed, high-enthalpy flow facilities. A critical factor for effective thrust production in a SCRAMJET is the efficient mixing of fuel with air and the subsequent chemical reactions that produce water. This article describes an experimental effort that measured the concentration of water at the exit plane of a simulated SCRAMJET in addition to using planar laser induced fluorescence (PLIF) of OH to visualize the mixing zone where hydrogen is injected into the Mach 3.0 flow. These results allow direct comparison of the degree of mixing near the hydrogen injector, as determined by the production of OH, with temperatures and concentration values for water 20 duct heights downstream of the injection station.

The results in this article are for the initial development of a nonintrusive diagnostic for line-integrated temperature and concentration measurements of water. The observed quantity is infrared (IR) emission from the ν_2 vibrational band centered at 6.27 μm, coupled with OH PLIF measurements in the near-injector zone of a high-enthalpy reacting flow. The flows were produced using a shock tunnel that generated Mach 3.0 flow with stagnation conditions ranging from 2500 to 3800 K. Mach 3.0 flow was verified using both pressure and schlieren measurements; boundary-layer effects were calculated and observed via schlieren measurements to be small. Two hydrogen-injector configurations were employed: 1) a dual-hole sonic wall injection system and 2) an axial injector that was specifically designed to be nearly velocity matched with the mainstream flow. Velocity-matched injection occurs at some point in the flight corridor for fixed geometry systems and presents a difficult operating regime from a mixing perspective. We have therefore chosen a near-velocity matched system for our axial injector.

In the following sections we describe the shock tunnel, the injection system, the OH PLIF measurements and methodology, the development of the water temperature and concentration measurement, and, finally, results from an initial test series with the two different injection geometries.

Shock-Tunnel Description

A full description of the shock tunnel and its operation has been previously published.[1] This initial publication describes the facility, its operating parameters, and presents wall-injection results for both helium and hydrogen injection. Optical measurements in the injection zone included schlieren as well as NO and OH PLIF. The shock tunnel is capable of generating stagnation temperatures far greater than those available using a conventional furnace or vitiated combustion methods. As currently configured, the shock tunnel is capable of simulating stagnation enthalpy for flight speeds below 3 km/s. The facility also includes a hydrogen injection capability that makes combustion tests possible for these flows. This system was carefully designed to provide on-demand injection and can be configured to test a variety of injector geometries. The shock tunnel was configured to operate at Mach 3.0 with a two-dimensional half-nozzle expanding to a 7.5-cm square cross section. The nozzle is followed by a 1.27-cm-high rearward-facing step in the floor of the tunnel and a replaceable injector block lies immediately downstream of this isolation step. Five orthogonal optical access stations are included along the shock tunnel so that both line of sight (LOS) and PLIF imaging measurements can be made. The first optical measurement station is immediately after the full expansion point for the nozzle and it includes three windows. Figure 1 illustrates the first three optical access stations along with the interchangeable injector block. The region immediately after the rearward-facing step includes two side windows that give full height optical access for a 14-cm flow length along with full laser access at the top of the tunnel.

Figure 2 illustrates the shock tunnel and diagnostics as configured for this test series. Three distinct optical measurements were included: 1) OH PLIF measurements in the injection/mixing zone, 2) water-vapor emission measurements at the exit plane, and 3) NO emission using a radiometer

Received May 12, 1993; revision received Feb. 15, 1995; accepted for publication Feb. 23, 1995.

*Principal Research Scientist, 20 New England Business Center; currently Associate Professor, Division of Engineering, Colorado School of Mines, Golden, CO, 80401-1887. Member AIAA.
†Principal Research Scientist, 20 New England Business Center. Member AIAA.
‡Senior Scientist, 20 New England Business Center. Member AIAA.
§Principal Scientist, 20 New England Business Center.
¶Manager Chemical Sciences, 20 New England Business Center.

Table 1 Injection and flow parameters

Injector	Stagnation Enthalpy, kJ/kg	Stagnation Pressure, atm	Tunnel flow Velocity, m/s	Tunnel flow Pressure, atm	Tunnel flow Temperature, K	Fuel equivalence ratio	Injector velocity, m/s	OH PLIF image figure no.	H_2O exit plane figure no.
Wall	3940	10.7	2120	0.27	1310	2.1	—	8	—
Wall	4200	11.6	2170	0.29	1360	2.1	—	9	13
Axial	2950	27.2	1930	0.68	1100	0.64	2270	11	—
Axial	4280	11.9	2184	0.30	1375	1.82	2270	10	14
Axial	5200	15.8	2330	0.40	1530	1.35	2270	12	—

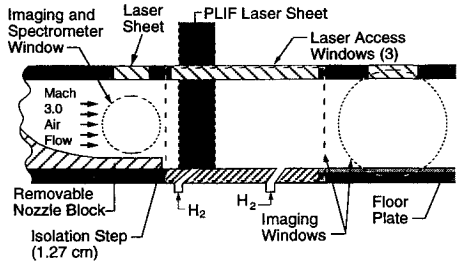

Fig. 1 Schematic diagram of optical access for the shock-tunnel test station.

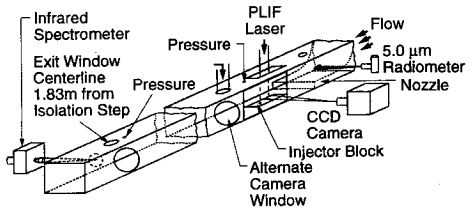

Fig. 2 Diagnostic setup for reacting flow tests.

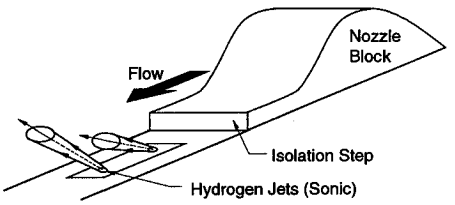

Fig. 3 Wall injection system.

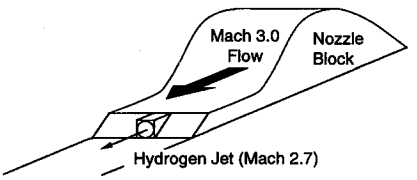

Fig. 4 Axial injection system.

centered at 4.95 μm and located at the nozzle exit. As described in a separate publication,[2] emission for the NO fundamental vibrational band originates near 5.3 μm. Its bandshape is temperature dependent; for temperatures between 1000–3000 K, the majority of the band radiance lies between 4.9–6.4 μm. The emission measurement centered at 4.95 μm, therefore, it was sensitive to NO vibrational temperature and column density. As described in both Parker et al.[1] and Rawlins et al.,[2] NO is formed in the high-temperature air present in the shock-tunnel plenum and remains at elevated levels at the exit of the Mach 3.0 nozzle. The radiance at 4.95 μm is, therefore, an accurate indicator for facility or "hot flow" test times. High-temperature flow duration is a critical performance parameter for impulse facilities such as shock tunnels and was determined to be between 1–2 ms using this radiometer.

Hydrogen Injection System and Injector Configurations

To produce reacting flows similar to those in a SCRAMJET, hydrogen must be injected into the shock-tunnel flow. The requirements for this are pulsed operation with a fast response time, near-constant injection flow rates during the shock-tunnel run time, and a reliable method of limiting the quantity of hydrogen injected into the system. This system has been previously described[1] and the two injector configurations used in this work are illustrated in Figs. 3 and 4. Overall system stoichiometry was calculated using one-dimensional gas dynamics for the system stagnation conditions (tunnel and injection flows) and sonic throat areas. The wall injection system consists of two 0.48-cm-diam ports located in the floor, along the tunnel centerline, at 2.3 and 8.4 step heights downstream of the rearward-facing step. The inlets were directed at 30- and 60-deg angles with respect to the tunnel flow. Pressure at the outlet orifices was calculated to be approximately 11 atm, assuming sonic flow at the exit plane. The axial injection system consists of three equal-width sections with the outer sectors machined to produce a 13.2-deg ramp between the step and the tunnel floor. The center sector consists of a backward-facing step with a nozzle in the downstream face. A simple 7-deg conical taper with a throat area of 0.317 cm^2 and an exit area ratio of 3.2 was used as the divergent portion of this nozzle. Pressure at the exit plane was calculated to be approximately 0.9 atm. This system was specifically designed to produce freestream and injection flow velocities of approximately equal magnitude. Table 1 lists stagnation conditions as well as relevant velocities and stoichiometries for four of the conditions examined in this work.

OH PLIF Measurements

The OH PLIF measurements were made using a Spectra-Physics Nd:YAG-pumped dye laser with frequency-doubling to 283 nm. The dye laser was modified for a larger spectral bandwidth by operating the grating in third order rather than fifth and adding a preamplifier cell. Using this approach, the frequency-doubled output of the dye laser was in excess of 0.6 cm^{-1}, more than twice that of the OH absorption linewidth. Between 6–10 mJ of laser energy was delivered to the test plane of the shock tunnel with 4.5- to 10.5-cm sheet widths and laser sheet thicknesses of approximately 0.05 cm. Fluorescence was imaged using an intensified camera system and was collected at right angles using a 105-mm uv lens operated at $f/4.5$ and filtered with carefully selected uv filter glasses. The filter glasses provided a long-pass cuton near 310 nm that rejected the laser elastic scattering from the tunnel floor. The intensifier was gated to ~20 ns around the ~10-ns laser pulse. This narrow gate width eliminated any chemiluminescent or thermal emission from the PLIF images. OH PLIF measurements were made in the near field for both injector configurations using the two optical access stations downstream of the rearward-facing step (as shown in Fig. 1).

The OH PLIF measurements were obtained by exciting the isolated $Q_1(7)$ transition at 283.29 nm. This transition was chosen because of its strength at the expected H_2–air combustion temperatures and our desire to have maximum sensitivity for these experiments. It should be noted that this frequency-doubled dye laser excitation of the (1, 0) band is in contrast to techniques that use excimer–laser excitation of the partially predissociative $v' = 3$ state.[3] For the levels of OH expected in our facility ($\sim 10^{15}$ cm^{-3}), it has been shown that the dye laser excitation strategy is preferable.[4]

The relationship between fluorescence signal and number density or mole fraction of OH has been described previously.[5] Briefly, the fluorescence is proportional to the laser energy, the fluorescence yield, the species number density, and the Boltzmann population fraction for the absorbing transition. In general, the fluorescence yield can have temperature, pressure, or gas-compositional dependencies. In regions of the flow with little pressure variation across the measurement plane, as in the downstream PLIF imaging station, the quenching term is essentially constant[6–9] and the PLIF image is a relative measure of the product of the OH number density and the temperature-dependent Boltzmann population term.[5] For $J'' = 7.5$, the population term is only weakly sensitive to temperature over the range of temperatures where OH is likely to be found (i.e., 1500–3000 K) and the relative uncertainty in number density across a nearly constant pressure image is approximately $\pm 10\%$ due to the Boltzmann temperature variations.

In flows with strong pressure variations, however, the fluorescence signal is better viewed as the ratio of the pressure-dependent OH number density and the pressure-dependent quenching term.[5] The fluorescence signal reduces to

$$S_F = \text{const} \cdot f_B/T \cdot \chi_{OH} \tag{1}$$

where

S_F = fluorescence signal
f_B = Boltzmann fraction
T = temperature
χ_{OH} = mole fraction of OH

Since the Boltzmann term at low J'' values is nearly temperature-independent, the ratio f_B/T is an inverse function of temperature. Hence, the fluorescence signal is proportional to the local mole fraction of OH with a factor of two variation from 1500 to 3000 K. It is possible to choose another transition so that the ratio f_B/T is essentially constant over some temperature range of interest so that, in strongly pressure varying flows, the fluorescence signal is directly proportional to species mole fraction. However, for these initial measurements, the increased sensitivity was deemed more important and we chose to accept the temperature variations in the strongly pressure-variant region of the flow in the vicinity of the dual wall injectors.

Measurements of H_2O Concentration and Temperature

A major thrust for this work was to develop a nonintrusive diagnostic suitable for monitoring the temperature and concentration of water in the exit plane of a high-enthalpy reacting flow system. The motivation for this measurement technique is quite clear; it will provide a direct measure of a combustion product and its temperature along a LOS at the combustor exit and will therefore provide a measure of combustor performance. The measurement relies on radiation from the ν_2 band centered at 6.27 μm and uses a custom-designed IR spectrometer system capable of acquiring synchronous spectra at a 125-kHz rate. This device consists of a liquid-nitrogen cooled HgCdTe linear detector array (Infrared Associates) interfaced to a 0.3-m, $f/6.2$ monochromator. The resulting spectral resolution is 0.19-μm/pixel. Each pixel in the array has a dedicated amplifier and digitizer providing a synchronous collection of spectra at data rates of 125 kHz. Data were acquired and processed through a multichannel data-acquisition system interfaced to a PC/AT computer. Absolute responsivity calibrations were performed with a temperature-controlled blackbody source. For the present measurements, the instrument was configured to obtain time-resolved, first-order spectra over the wavelength range 6.5–8.55 μm. The field of view (FOV) of the spectrometer was controlled by imaging the entrance slit into the center of the shock-tunnel exit plane. The image size at the tunnel centerline was a 3.1-mm square. The emission measurement integrated along a LOS, and due to the finite angle for the collection optic, the collection area on each side of the shock tunnel was a 6.6-mm square. Due to the strong absorption strength of atmospheric water in this spectral region the spectrometer and imaging optics assembly were purged with dry nitrogen. The unpurged path length in the atmosphere was 7 cm and this length was shown to produce insignificant absorption for wavelengths greater than 6.5 μm. This conclusion is supported by a comparison of the spectrometer calibrations performed in high and low relative-humidity environments.

Prior to implementation of the system on the shock tunnel, the observed radiances and bandshapes were calibrated for H_2O concentration and temperature by recording emission spectra from an incident shock-heated mixture of argon, hydrogen, and oxygen (85, 10, 5%). The measurements were performed at near 1-atm pressures in a 10.4-cm diam shock tube using previously prepared gas mixtures of ultra-high purity (UHP) argon, hydrogen, and oxygen. The reacting system was modeled using an incident shock chemical kinetics package produced by Sandia (DSHOCK)[10] and calibration temperatures and concentrations were carefully extracted from the pseudo-steady-state region following an initially reactive period.

Relative calibration spectra, shown in Fig. 5, illustrate the increased radiances for long wavelengths at elevated temperatures that are typical of increased thermal populations in upper vibrational states. The vibrational temperature for the water can therefore be determined by monitoring the relative shape of the emission spectrum while the concentration is determined by monitoring the absolute radiance in one of the bandpasses. In order to produce a systematic temperature and concentration measurement methodology we have assumed that the radiance in each bandpass follows the functional form given in Eq. (2):

$$N_\lambda/[H_2O]l = \alpha_\lambda e^{-\beta_\lambda/T} \tag{2}$$

where

N_λ = system radiance at wavelength λ
$[H_2O]$ = concentration of water molecules
l = path length
T = temperature
α_λ, β_λ = empirically determined constants

The characteristic exponential slope β_λ increases with wavelength as would be expected from the spectra shown in Fig. 5. Inspection of Eq. (2) reveals that ratios of radiances at two wavelengths are sensitive to temperature only and are independent of concentration. Equation (3) formalizes this relationship and provides a direct means of calculating temperature. The values of α_λ and β_λ are determined using a least-squares fit of the calibration observations to Eq. (2). Therefore, observed radiance ratios can be used to determine the temperature via Eq. (3) and column density ($[H_2O]l$) using Eq. (2).

$$T = \frac{\beta_{\lambda_1} - \beta_{\lambda_2}}{\ln[(N_{\lambda_1}/N_{\lambda_2})(\alpha_{\lambda_2}/\alpha_{\lambda_1})]} \tag{3}$$

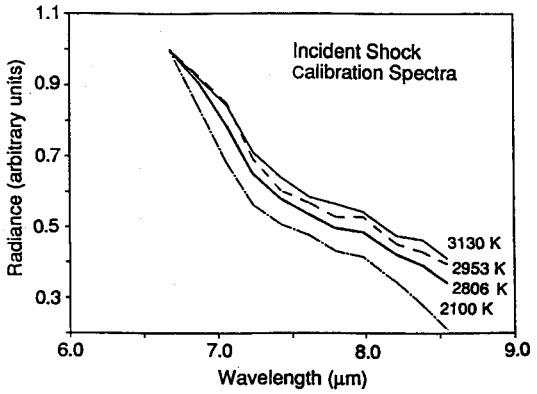

Fig. 5 Normalized calibration spectra for water.

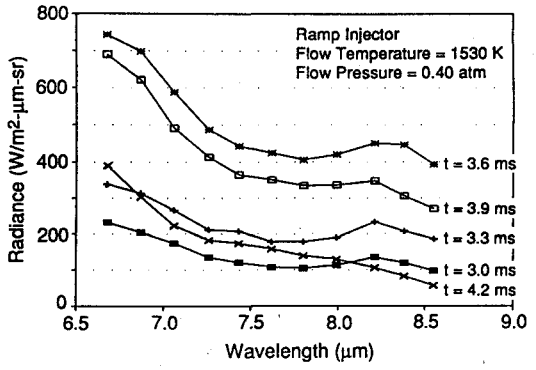

Fig. 6 Time-resolved spectra from the shock-tunnel exit plane.

The specific bandpass wavelengths that are used for temperature and concentration determination are important for the shock-tunnel data. Figure 6 illustrates sample spectra at the exit plane of the shock tunnel for a combusting flow. These spectra include a feature centered at 8.25 μm that was not apparent in the shock-tube calibrations. This feature is either due to a molecular radiator that was not present in the shock-tube calibrations (which included no nitrogen), or is indicative of vibrational nonequilibrium for the radiating water. Although one cannot rule out vibrational nonequilibrium, vibrational relaxation rates from $v_2 = 1$ to $v_2 = 0$ are relatively fast.[11] For 2500 K, 0.3-atm conditions in the tunnel, the half-life of the $v_2 = 1$ state is approximately 7 ns. This indicates that our system should be in vibrational equilibrium. For the present data, temperature was determined using the bandpasses centered at 6.68 and 7.43 μm. Concentration was determined using this temperature and the radiance from 6.68 μm. These wavelengths were selected to provide the highest sensitivity in the temperature calculation, whereas the concentration calculation was specifically chosen to be insensitive to temperature.

Finally, a note on the accuracy of the temperature and concentration measurement is in order. This diagnostic is currently being developed and the calibration data set is not large enough to produce system constants that are highly specified. The absolute accuracy for the current radiometric data is approximately 30% and is dominated by uncertainties in the determined values of β_λ for our calibration set. However, careful implementation of a comprehensive calibration matrix and carefully executed chemical kinetic modeling would permit the use of higher-order terms in Eq. (2) and bring the absolute accuracy to approximately 5–10%, which is typical for carefully calibrated absolute radiance measurements. Temperature comparisons within a data set are limited by the noise in the radiometric signals. In all cases, the signal levels used in this work had signal to noise ratios (SNRs) between 10–50. The relative uncertainty in temperature, as calculated using an rms sum of errors based on Eq. (3), is approximately 20% for the wavelength pair 6.68 and 7.43 μm. Relative uncertainties in concentration, as calculated using Eqs. (2) and (3), for a 3000-K system are also roughly 20% for typical SNRs. Continuing efforts to refine the calibration data set and extend the measurements to longer wavelengths indicate that temperature accuracies of 5–10% and concentration accuracies of 10–20% can be achieved.

Results and Discussion

The data acquired as a part of this test series include four basic flow conditions, as described in Table 1, and results from each of these conditions are presented in this article. However, before discussing these images and the exit plane water measurements, a brief discussion of the flow and timing in the shock tunnel is necessary. Figure 7 illustrates the signals from a reacting-flow test and shows the pressure in the injector plenum, the signal from the radiometer at the nozzle exit, and the pressure on the top wall immediately following the injector station. Also included in this figure are the injector times and PLIF laser pulse. Features to note in this figure are the clear demarcation of the flow test time by the radiometer, the relatively stable pressure trace following the injector station, and the constant pressure in the injector plenum during the flow time. In addition, note that tunnel pressure and radiance signals are not coincident in space (separation is 0.30 m) and, therefore sample, at a given instant, different portions of the flow.

Figure 8 is an image of the OH distribution in the immediate vicinity of the first injector of the dual-hole, wall-injector system. In this and all other images, the flow is from left to right and the relative fluorescence signal levels are grey-scale encoded with increasing darkness corresponding to increasing quantities of OH. Also, in each image, the bottom of the PLIF image corresponds to the bottom wall of the tunnel. The FOV in Fig. 8 is 80 mm (H) by 60 mm (W) and the left side of the image is just upstream of the first injector. A low, fairly uniform level of OH in the recirculation zone/boundary

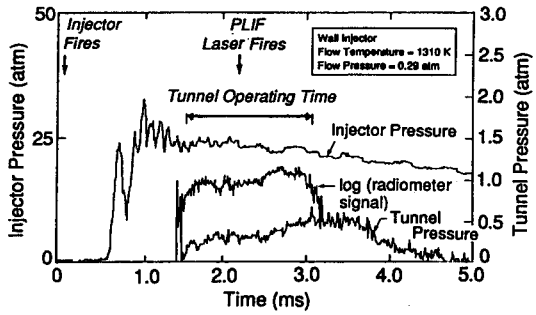

Fig. 7 Injection pressure, tunnel pressure, and radiometer signal for a reacting flow measurement.

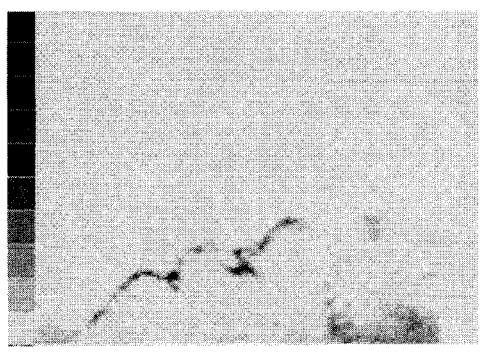

Fig. 8 OH PLIF image above the first side-wall injector, flow temperature = 1310 K.

layer upstream of the injector is visible in the lower-left-hand corner of the image. A thin filament of OH, on the order of 1 mm thick, attaches very near the recirculation zone and extends away from the wall along an irregular line, indicative of the mixing zone between the high-speed injectant flow and the freestream flow. Based upon a freestream Reynolds number of approximately 5×10^6/m and a jet Reynolds number of 9×10^7/m, this mixing zone is expected to be turbulent. This is further supported by the shape of the mixing zone that is "wavy" in structure with length scales of up to 7 mm. Earlier studies[5] have shown that just upstream of this OH zone lies the bow shock generated by the interaction of the injectant plume and the freestream flow. The light regions above this thin filament, of course, correspond to the freestream flowfield where no hydrogen and air mixing has occurred. The center of the fuel plume itself is also light, indicating no mixing and OH formation. Downstream and underneath the fuel plume, between the two injectors along the tunnel floor, significant amounts of OH are observed in a spatially extended, reasonably well-mixed zone.

Figure 9 is a similar image from another test, taken with a larger FOV, observing a region 105 by 79 mm. Again, the left side of the image is just upstream of the first injector position. This image also clearly shows the thin OH filament between the first injector and the freestream flow. The large FOV, however, encompasses the second injector station and more clearly shows the large, well-mixed levels of high OH concentration between the two injectors. The right side of this image corresponds to the second injector station and shows an abrupt disappearance of the OH at the second H_2 plume. A second thin filament, due to the second injector, is observable in this image. Both images indicate that the thin OH filament is typically on the order of 1 mm thick, although it fluctuates spatially with the turbulence motion in observable scales up to about 7 mm in diameter. The region between the jets also displays turbulent mixing as evidenced by the variation in OH signal levels. The first jet penetrates to an average height of 16 mm (defined by the edge of the OH filament) before fully aligning with the freestream flow.

Using the fluorescence model presented previously and assuming nominal conditions of 0.5 atm and 2000 K, the peak OH fluorescence signal in the thin filament between the fuel jet and the freestream corresponds to an OH number density of about 1×10^{15} cm^{-3}, or about 500 ppm. The pressure and temperature fields in this portion of the flowfield are very complex. The nominal conditions are reasonable for the OH in the filament above the fuel jet where the pressure should be on the order of the freestream static pressure and the temperature, reflecting some initial heat release, should lie between the freestream and adiabatic flame temperatures. Below the fuel jet and between the two injectors, however, flow velocities must be significantly reduced, which implies an increase in the local pressure. Since we have not yet measured the pressure or temperature variations in this flow, we can only bound the uncertainty in quantitatively interpreting the relative fluorescence signals in this image in terms of the relative OH number density, or mole fraction. The pressure in this region may vary from near the freestream value to near the postbow shock pressure, or from about 0.5 to about 4 atm. The temperature at which OH is likely to be found was discussed in the previous section and we observe that, in the stagnation region upstream of the second injector station, the bulk gas temperature may approach the stagnation temperature of ~3500 K.

The highest fluorescence signals originate in the large, well-mixed portion of the flow where the temperatures and pressures are substantially higher than the nominal conditions used to estimate the OH concentration in the flame filament. The peak signal levels here are two to three times higher than in the filament. Considering the mole-fraction sensitivity of the fluorescence signal (which is independent of pressure), one expects the fluorescence signal at constant mole fraction to decrease by about a factor of two from the nominal filament temperature (1500 to 2000 K) to the stagnation temperature (approximately 3500 K). Combining the increased signal levels and the decreased absorption strength at higher temperature, the peak mole fraction estimated in the region between the two injectors was on the order of 2000–3000 ppm, or 0.2–0.3% of the total number density. These numbers are comparable to equilibrium values for hydrogen/air combustion at these temperatures and are reasonable for this portion of the flowfield, particularly considering the relatively long residence time available for the fuel and air to mix on a molecular level in the slow flow between the injectors.

The flame zone in the upper filament, as viewed by the OH fluorescence, is intermittent and the detection limit for the nominal conditions is about 1×10^{13} cm^{-3}, or 5 ppm. Hence, intermittency is determined in this case by the OH concentration falling below this level, compared to a peak level of approximately 1×10^{15} cm^{-3}. The PLIF images of Figs. 8 and 9, therefore, do not necessarily indicate a discontinuous flame zone, but rather indicate a flame zone with a minimum of two decades of variation in OH concentration.

The remaining PLIF images all correspond to the axial injection condition and were obtained 29 cm downstream of the injector exit plane. Figure 10 is a PLIF image at the similar flow condition to Figs. 8 and 9 and corresponds to a FOV of 45 by 34 mm. In these images, the injectant hydrogen velocity was nearly matched to the freestream centerline velocity above the injector. The OH filament separating the fuel jet from the freestream is typically less than 1 mm thick and fluctuates spatially as it progresses downstream. Several thick or concentrated OH zones are present along the top filament and the spatial variation in OH concentration indicates turbulent mixing both above and below the fuel jet. The calculated Reynolds number for the fuel jet is ~10^6, based on the outlet diameter, which indicates the flow should be turbulent. It is also notable that no extinction of the flame sheet is observed.

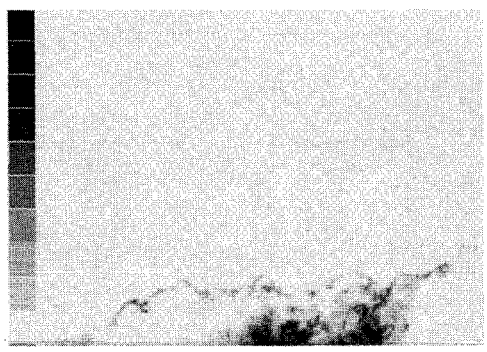

Fig. 9 OH PLIF image above both side-wall injectors, flow temperature = 1360 K.

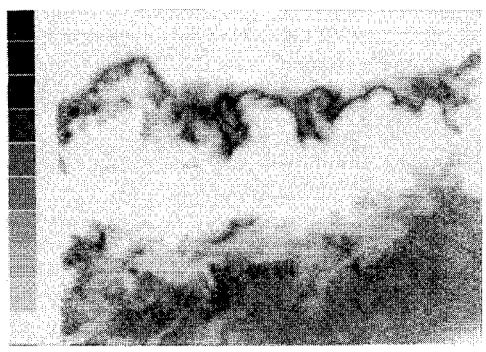

Fig. 10 OH PLIF image downstream of axial injector, flow temperature = 1375 K.

The light region below the flame sheet corresponds to the fuel jet itself, which measures approximately 12 mm in diameter, essentially the same as the injector jet diameter. The position of this jet above the tunnel flow, however, fluctuates with downstream distance. The mean position of the jet centerline height is about 20 mm, significantly higher than the centerline exit height of 6.4 mm.

In marked contrast to the interface between the fuel jet and the freestream, the region between the fuel jet and the wall shows a much thicker mixing layer. Significant freestream air entrainment and mixing is evident by the large quantities of [OH] in this region. The picture that emerges from this image is that of a fuel jet lifting away from the wall and vigorously mixing underneath. The peak OH levels in these images are again on the order of $2-3 \times 10^{15}$ cm^{-3}. Since the pressure across this image is reasonably constant, we can more accurately relate the fluorescence signal variations to number density variations than in the images above the side-wall injectors. The OH formation per unit volume is similar everywhere in this image to the thin filaments above the side wall injectors, although the total OH produced in the image (proportional to the total hydrogen conversion) is much greater due to the vigorous mixing below the jet.

Figure 11 is an OH PLIF image at the same station with a different FOV and flow conditions as given in Table 1. In Fig. 11, the FOV is increased to 60 × 45 mm and the velocity difference between the fuel jet and freestream is nearly 300 m/s (the fuel jet velocity is greater than that of the freestream). This image reveals a very different mixing pattern for the fuel jet. Instead of a clearly defined fuel jet with a thin filament separating the jet from the freestream, vigorous mixing has occurred above and below the jet. Indeed, the jet itself is almost indistinguishable, with measurable OH throughout its diameter. The lifting of the fuel jet into the freestream is difficult to precisely quantify due to mixing throughout the jet, but is approximately the same as that in Fig. 10. It is interesting to note "pockets" of high OH concentration in the center of the jet. One can postulate that these pockets originate at the top or bottom of the jet and have moved to the jet centerline. Mixing and total OH formed within the image are substantially higher than in Fig. 10. The sensitivity in these images is the same as in Fig. 10, indicating peak concentrations on the order of 10^{15} cm^{-3}. It is interesting to note that the increased velocity difference of the fuel jet/freestream shear layer results in intermittency of the flame sheet.

A last PLIF image was obtained at the same location and is shown in Fig. 12, now with the freestream gas temperature over 1500 K and a velocity over 2000 m/s. In contrast to the case shown in Fig. 11, the freestream velocity now exceeds the jet exit velocity; the magnitude of the velocity mismatch is approximately 50 m/s. The OH distribution in Fig. 12 reveals a mixing pattern very similar to that of Fig. 10 (the FOV is identical to Fig. 10), although the highest signal levels are now in the thin filament between the fuel and the freestream

Fig. 11 OH PLIF downstream of axial injector with velocity mismatch, flow temperature = 1100 K.

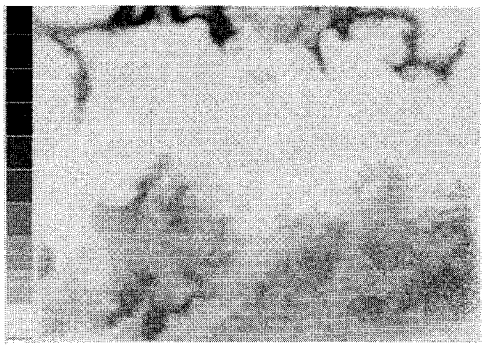

Fig. 12 OH PLIF image downstream of axial injector with high-speed freestream, flow temperature = 1530 K.

rather than between the fuel and the wall. The penetration of the jet into the freestream is noticeably improved, with the outer OH boundary extending 34 mm above the tunnel floor.

Results for the three axial injection conditions just discussed allow a comparison of the effect of initial velocity difference on the mixing/combusting field 23 jet diameters downstream of the injector outlet. Figures 10 and 11 are OH PLIF images for a freestream velocity that is 90 and 340 m/s less than the jet velocity, whereas Fig. 12 is for freestream velocity 50 m/s more than the jet velocity. In all of these images the jet lifted substantially off the tunnel floor similar to the results of Waitz et al.[12] Precise specification of jet height is difficult to quantify due to spatial variations in the jet; approximate centerline heights are 19, 17, and 22 mm for Figs. 10, 11, and 12 respectively.

This set of OH images for the axial injection, Figs. 10, 11, and 12, can be separated into two behaviors. For an initial jet to freestream velocity mismatch of less than 100 m/s, mixing/burning zones are apparent both above and below the jet. When the velocity mismatch is increased to approximately 300 m/s, the mixing includes the entire jet height with higher OH concentrations at both the top and bottom of the fuel-rich stream.

One must remember that the flow and mixing field are three dimensional in nature, and therefore, direct comparison to results from two-dimensional shear layers is not possible. In all cases the convective Mach number based on the initial velocity differential is small; the 340-m/s differential has a convective Mach number of 0.17 vs 0.04 or less for the near-velocity matched cases. As the results show, mixing and combustion are not simply due to the entrainment of one stream into another as with two-dimensional shear layers. Mixing is dramatically affected by jet lifting off the tunnel floor since the region below the jet in all cases contains OH from the jet boundary to the tunnel floor. The mechanism for this liftoff can be both baroclinic torque from the flow turning shocks on either side of the jet,[12] and vorticity generation from misaligned freestream and axial-jet velocity vectors.[13] Clearly, the three-dimensional nature of this flowfield is exceptionally important in controlling the overall mixing/combustion behavior.

Figures 13 and 14 show the results from the time-resolved, H_2O temperature and concentration measurements as well as idealized temperatures and column density predictions. These results are for the wall-injection system and axial injector at similar flow conditions as listed in Table 1. Figure 13 illustrates the temperature and column density profiles for the two-hole wall-injection system. This plot uses the 125-KHz spectral data with a three-point running average to remove spurious noise. Several features are prominent in this figure. First, the end of the test time is clearly shown by a steep drop in the temperature of the water. The length of the test time, as defined by the IR radiometer at the nozzle exit, is used to identify the beginning of the flow time at this optical station.

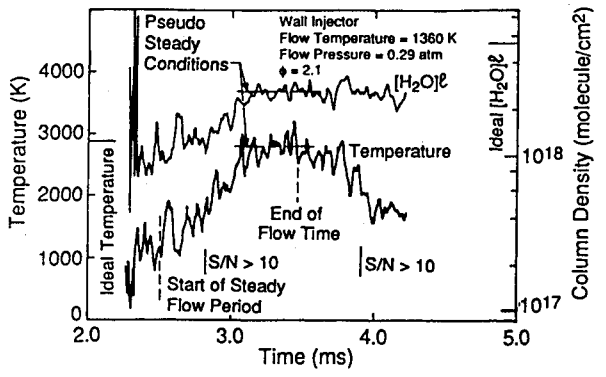

Fig. 13 Wall injection exit plane results.

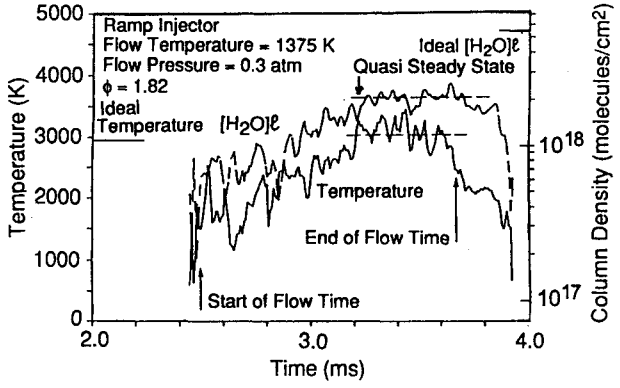

Fig. 14 Axial injection (with velocity matching) exit plane results.

This time is consistent with the expected arrival time of the hot gas slug based on the distance between the measurement stations and convective velocity in the tunnel. This figure is also marked to note the region where the SNRs rise above the 10:1 level. Both temperature and column density start at relatively low values and after approximately 1 ms asymptote to relatively steady conditions. This is an important observation since it supports the hypothesis that pulsed, short-duration flow facilities can be used to study the steady-state properties of these high-temperature reacting flows. The observed exit plane temperature is approximately 2700 K with an H_2O column density of (2 to 3) $\times$ 10^{18} molecules/cm^2.

Figure 13 also includes idealized temperature and column density predictions. These predictions are based on a simplified model that creates an initial, fully mixed starting condition based on the air- and hydrogen-injection flows and then allows this system to react as it flows down the duct. This prediction follows the temperature, pressure, species concentrations, and velocity as a function of relative axial position in the duct. The starting condition for this calculation is determined by specifying a completely homogeneous system with the pressure, temperature, and velocity imposed by conserving mass, momentum, and enthalpy from the inlet air and hydrogen flows (note that the momentum of the hydrogen for the wall injection system was neglected since it was not totally oriented in the downstream direction). The initial chemical composition is chosen to reflect the exit composition of the air and hydrogen flows. Results from these calculations provide a comparison for the exit temperature and column density measurements. In all of the experimental cases, the agreement between predicted and observed temperatures was excellent. However, the agreement in predicted and measured column densities is less consistent.

The column density observed in Fig. 13 was approximately 45% of the idealized value. This discrepancy could be due to either incomplete mixing, and therefore, incomplete product formation, finite rate chemistry that would slow the rate of product formation, or variations in the gas composition at the exit plane. Unfortunately, our measurements for this effort did not include reliable pressure measurements at the exit plane. In all cases, pressure measurements are clearly biased by a heating of the piezoelectric transducer that produces a continuous drift in the pressure signal during the experiment. In the future, this problem will be corrected by coating the transducer with a silicon rubber so that it will not be directly subjected to the high temperatures and velocities of the exit plane.

Figure 14 illustrates the results for an axial injection system operated at conditions identical to that for Fig. 13 (wall-injection system). The observed column density for this system is very similar to that observed for the wall injector. In each of the two cases, the observed column density was approximately 45% of the idealized values, which indicates that the mixing of the velocity matched axial system was equivalent to that of the wall injection system. If the mixing for one of the systems was exceptionally poor, the result would be decreased water in the exit plane of the combustor. Unfortunately, this conclusion must be tempered by the absence of a pressure measurement that would allow a complete comparison between the two data sets. However, it is encouraging that the results for the velocity-matched axial system and the wall injection system are similar.

Conclusions

This study has demonstrated nonintrusive optical measurements of the operation and performance for wall- and axial-hydrogen injectors in simulated SCRAMJET flows. Specific measurements applied to this system were 1) PLIF imaging of OH in the near-injector region; 2) LOS emission monitoring of H_2O at the exit plane that produced temperatures and column densities for the flow; and 3) LOS emission monitoring for NO in the entrance flow to quantify test time duration. Specific conclusions from these measurements are as follows:

1) A fast-gating camera (approximately 20 ns) was shown to effectively eliminate emission from the fluorescence images.

2) PLIF images of OH for the wall injection system indicated a flame sheet attached to the recirculation zone behind the rearward-facing step. This flame sheet was approximately 1 mm thick and exhibited spatial structures with length scales up to 7 mm in size. An intense reaction zone was observed between the two injector jets with peak OH mole fractions greater than 0.1%.

3) Ignition occurred further downstream from the axial injectors than for the comparable conditions for the wall injection system. OH PLIF measurements of the mixing zone show jet liftoff from the tunnel floor for velocity mismatches of 50, 90, and 340 m/s. OH was observed throughout the jet centerline for a velocity mismatch of 340 m/s, compared to no OH at the jet centerline for velocity mismatches below 100 m/s.

4) Exit plane measurements of temperature were in excellent agreement with a simplified one-dimensional model of the system. In addition, measurements of water column density indicated that a quasisteady state was achieved during the 1- to 2-ms test times.

Acknowledgments

This work was supported by the U.S. Air Force under Contract F33615-91-C-2204, Kervyn Mach, monitor. We also appreciate discussions with G. Burt Northam of NASA Langley on fuel injection geometries.

References

[1]Parker, T. E., Allen, M. G., Reinecke, W. G., Legner, H. H., Foutter, R. R., and Rawlins, W. T., "High Temperature Supersonic Combustion Testing with Optical Diagnostics," *Journal of Propulsion*

and Power, Vol. 9, No. 3, 1993, pp. 486–492.

[2]Rawlins, W. T., Parker, T. E., Foutter, R. R., and Allen, M. G., "Time-Resolved Infrared Emission Spectroscopy in High Enthalpy Supersonic Air Flows," *AIAA Journal*, Vol. 31, No. 3, 1993, pp. 499–504.

[3]Quagliaroli, T. M., Laufer, G., Krauss, R. H., and McDaniel, J. C., Jr., "Planar Imaging of OH Density Distributions in a Supersonic Combustion Tunnel," AIAA Paper 93-0042, Jan. 1993.

[4]Seitzman, J. M., and Hanson, R. K., "Comparison of Excitation Techniques for Quantitative Fluorescence Imaging of Reacting Flows," *AIAA Journal*, Vol. 31, No. 3, 1993, pp. 513–519.

[5]Allen, M. G., Parker, T. E., Reinecke, W. G., Legner, H. H., Foutter, R. R., Rawlins, W. T., and Davis, S. J., "Fluorescence Imaging of OH and NO in a Model Supersonic Combustor," *AIAA Journal*, Vol. 31, No. 3, 1993, pp. 505–512.

[6]Smith, G. P., and Crosley, D. R., "Vibrational Energy Transfer in $A^2\Sigma^+$ OH in Flames," *Applied Optics*, Vol. 22, No. 10, 1983, pp. 1428–1435.

[7]Garland, N. L., and Crosley, D. R., "On the Collisional Quenching of Electronically Excited OH, NH, and CH in Flames," *21st Symposium (International) on Combustion*, The Combustion Inst., Pittsburgh, PA, 1986, pp. 1693–1702.

[8]Drake, M. C., and Pitz, R. W., "Comparison of Turbulent Diffusion Flame Measurements of OH by Planar Fluorescence and Saturated Fluorescence," *Experiments in Fluids*, Vol. 3, 1985, pp. 283–292.

[9]Barlow, R. S., and Collignon, A., "Linear LIF Measurements of OH in Non-Premixed Methane-Air Flames: When are Quenching Corrections Unnecessary," AIAA Paper 91-0179, Jan. 1991.

[10]Mitchell, R. E., and Kee, R. J., "A General-Purpose Computer Code for Predicting Chemical Behavior Behind Incident and Reflected Shocks," Sandia National Labs., Sandia Rept. SAND82-8205, Livermore, CA, Feb. 1991.

[11]Lewis, P. F., and Trainor, D. W., "Survey of Vibrational Relaxation Data for O_2, N_2, NO, H_2, CO, HF, HCL, CO_2, and H_2O," Advanced Research Projects Agency, AVCO Everett Research Lab., Inc., Rept. 1092, Everett, MA, Nov. 1974.

[12]Waitz, I. A., Marble, F. E., and Zukoski, E. E., "Investigation of a Contoured Wall Injector for Hypervelocity Mixing Augmentation," *AIAA Journal*, Vol. 31, No. 6, 1993, pp. 1014–1021.

[13]Manning, T. A., "Experimental Studies of Mixing Flows with Streamwise Velocity," M.S. Thesis, Dept. of Aeronautics and Astronautics, Massachusetts Inst. of Technology, Cambridge, MA, Sept. 1991.